MDPI

Article

Experimental and Numerical Simulation Investigation of Cement Sheath Integrity during Multi-Stage Fracturing in Offshore Tight Oil Reservoir

Yangang Wang and Yongcun Feng *

College of Petroleum Engineering, China University of Petroleum (Beijing), Beijing 102249, China;
2019310110@student.cup.edu.cn
* Correspondence: yfeng@cup.edu.cn

Abstract: The integrity of the cement sheath is susceptible to failure during multi-stage fracturing. In this study, the failure mechanisms of cement sheath integrity during multi-stage fracturing in the A offshore tight oil reservoir wells were investigated. The cement samples were subject to triaxial compression test (TCT), triaxial cyclic loading test (TCLT), and permeability test. A full-scale device was constructed for cement sheath integrity experiments. Additionally, a 3-D finite element model was developed to simulate the interface debonding and the subsequent growth of micro-annuli throughout multi-stage fracturing. The results revealed that TCLT induced cumulative plastic deformation in the cement samples, resulting in a 10.7% decrease in triaxial compressive strength, an 8.3% decrease in elastic modulus, and a 150% increase in permeability. Despite these significant variations, no serious damage was caused to the cement sheath matrix. It was observed that gas leakage occurred at the 8th, 10th, and 14th cycles under cyclic loading with upper limits of 70 MPa, 80 MPa, and 90 MPa, respectively. After 15 cycles, the experimentally measured widths of micro-annuli were 117 μm, 178 μm, and 212 μm, which were in good agreement with simulation results of 130 μm, 165 μm, and 205 μm, respectively. These findings elucidate the causes of cement sheath integrity failure, providing insights into the failure mechanisms of cement sheath integrity during multi-stage fracturing.

Keywords: offshore tight oil reservoir; multi-stage fracturing; cyclic loading; cement sheath integrity

1. Introduction

Global demand for oil and gas has witnessed a substantial increase in recent decades [1]. As the global development of oil and gas reservoirs with medium to high permeability intensifies, the depletion of high-quality hydrocarbon resources is becoming increasingly evident [2]. Consequently, there is a growing interest in unconventional resources [3]. The exploration of unconventional oil and gas resources, particularly tight and low-permeability reservoirs [4], has steadily expanded and undergone extensive development worldwide [5].

Multi-stage fracturing technology significantly enhances the productivity of oil and gas wells by creating complex fracture networks within reservoirs, making it the most effective method for exploiting unconventional resources, such as tight and low-permeability formations [6]. Offshore unconventional resources, including tight oil reservoirs, constitute a substantial proportion of the world's hydrocarbon potential and necessitate multi-stage fracturing techniques to increase productivity [7].

However, the integrity of the cement sheath is susceptible to failure during multi-stage fracturing, leading to sustained casing pressure (SCP). It poses threats to the safe production of oil and gas wells and potentially causes environmental and safety issues during subsequent drilling operations [8]. Consequently, the sustainable development of unconventional oil and gas reservoirs is compromised [9]. Understanding the key factors affecting cement sheath integrity in multi-stage fracturing is crucial [10]. Therefore, it is

imperative to explore the mechanisms behind cement sheath integrity failure during multi-stage fracturing, thus providing a basis for the rationalization of fracturing construction parameters [11].

During multi-stage fracturing, variations in internal pressure within the casing induce alternating stresses in the cement sheath, serving as a primary factor contributing to its integrity failure [12]. In addition, the mechanical environment around the cement sheath becomes more complex during multi-stage fracturing due to abrupt changes in casing pressure and temperature [13]. This complexity makes it challenging to mathematically analyze and physically simulate cement sheath integrity failures under such conditions [14].

The causes of cement sheath integrity failure can be categorized into three types: disking cracks, radial cracks, and debonding. Disking cracks and radial cracks are typically induced by mechanical stresses, whereas debonding is usually caused by the mismatched deformation between the casing and the cement sheath [15].

Goodwin and Crook [16] conducted a laboratory test to investigate the integrity of a casing–cement–casing system. They observed catastrophic shear failure and the formation of radial cracks in the cement sheath under alternating pressure loading conditions. Kuanhai et al. [17] designed a simulated wellbore device for evaluating cement sheath integrity under different pressures. The findings of this study offered valuable insights into the impact of pressure on the mechanical properties of cement sheath interfaces. Su et al. [18] developed a mechanical equivalence method to replicate the wellbore loading on the cement sheath using a self-designed wellbore simulator. Cyclic load tests were conducted, revealing a decrease in the tensile strength of the cement sheath following cyclic loading. Feng et al. [19] and Wang and Taleghani [20] developed a combined numerical model for simulating hydraulic fracturing processes. They observed that fluid pressurization may create cracks in the annular space around the wellbore, specifically between the cement sheath and the formation. This phenomenon subsequently leads to the formation of channels conducive to gas flow.

Li et al. [21] constructed a comprehensive physical simulation experiment to identify the primary determinant in scenarios involving cyclic loading and unloading. The results revealed that plastic strain accumulates throughout the cyclic loading and unloading process, leading to the formation of micro-annuli at the primary interface, which then served as channels for gas migration.

In the previous study investigating the integrity of cement sheath, the material was considered to be elastically brittle with stresses influenced by its properties [22]. Pereira et al. [23] also explored the reduction of shear failure in cement sheaths during hydraulic fracturing, suggesting that lowering the elastic modulus can mitigate this type of failure.

Landry et al. [24] found that in a shale gas field in the USA, SCP always occurs after fracturing and occasionally before fracturing. They attributed the predominance of SCP to issues such as improper cement placement or incomplete consideration of stimulation conditions. Additionally, they emphasized the importance of considering changes in cement sheath stress during stimulation and throughout well operation.

During multi-stage fracturing, the pressure inside the casing frequently rose and fell, subjecting both the casing and the cement sheath to cyclical loading [25]. Earlier research has shown that while the cement sheath might withstand a static load, it is prone to failure under repeated applications of the same load, typical of the pressure fluctuations experienced in multi-stage fracturing [26].

Ramadan et al. [27] developed a wellbore model to simulate gas migration in the cemented annulus. A series of tests were performed using this model to assess the sealability of both neat Class H and Class G cement types. Various additives, including bentonite and latex, were incorporated. The tests demonstrated that the permeability of annulus cement in the wellbore increased as the cement aged.

A strong bond between the casing and cement sheath is essential to mitigate the occurrence of micro-annuli leakage paths at their interface [28]. Various elements, such

as the cement type, the surface condition of the casing steel, and the curing environment, significantly affect the bond strength between these materials [29]. Furthermore, the evaluation of the bond strength between casing and cement sheath commonly involves the implementation of laboratory pushout tests [30].

Tabatabaei et al. [31] conducted pushout tests to assess the effect of surface-modified cement additives incorporating graphite nanosheets on bond strength under various scenarios involving oil-based mud residues.

Corina et al. [32] examined the sealing effectiveness of neat and silica–cement systems in pipes with three varying degrees of surface roughness. In their study, gas leaks were identified in all samples at low differential pressures, demonstrating that the cement–casing interface is the source of these leaks.

The tight oil reservoir A is located in offshore China, and all of its production wells utilize a typical three-casing structure. Among them, the structure of Well H is depicted in Figure 1. After multi-stage fracturing, several wells have exhibited SCP, all of which occurred in the B annulus (the space between the production casing and intermediate casing). This phenomenon indicates a failure of the cement sheath integrity within the B annulus. Thus, investigating the underlying mechanisms responsible for compromising the integrity of the cement sheath in the B annulus constitutes the primary focus of this study.
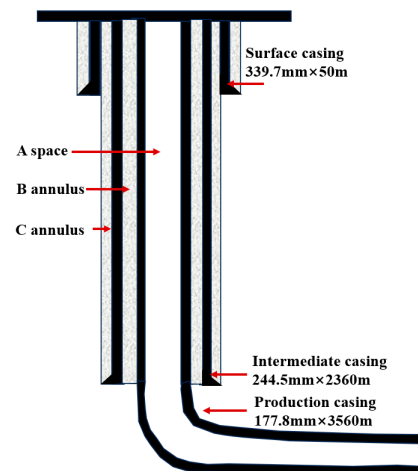

Figure 1. Structure of Well H.

This study aims to investigate the failure mechanisms of cement sheath integrity during multi-stage fracturing in the A offshore tight oil reservoir wells. The cement samples were subjected to triaxial compression test (TCT), triaxial cyclic loading test (TCLT), and permeability test. It quantifies the cumulative plastic deformation pattern of the cement under cyclic loading, assesses the impact of cyclic loads on the mechanical properties and permeability of the cement, and experimentally examines the failure of cement sheath integrity under multi-stage fracturing conditions using a full-scale device. The morphology of the micro-annuli was observed using a scanning electron microscope (SEM), and the widths of the micro-annuli were precisely measured. Based on the actual geological conditions and wellbore structure, a 3-D finite element model was developed to simulate the development of cumulative plastic strain, interface debonding, and the growth of micro-annuli during multi-stage fracturing.

The numerical simulation results are in good agreement with the experimental results, providing valuable insights for a more in-depth understanding of the failure mechanisms and patterns associated with the cement sheath integrity during multi-stage fracturing. This study also provides guidance for the rational design of fracturing parameters.

2. Physical Experiments

2.1. Mechanical and Permeability Testing of Cement

The test cement was formulated using 100% G-grade cement, 23% silica fume, 6% anti-gas channeling agents, 4.5% fluid loss additive, 1.0% retarder, and 0.3% dispersion agent, with a 0.4 water-to-cement ratio and a 1.84 g/cm^3 density. The cement slurry was then cured to obtain cement stone. This cement stone was standardized for cylindrical specimens, measuring 25 mm in diameter and 50 mm in height, as depicted in Figure 2a for samples 1 and 2. These specimens had consistent mechanical and permeability characteristics. Initially, the initial permeability of sample 1 was evaluated using nitrogen gas as the testing medium, as illustrated in Figure 2b, followed by a TCT in Figure 2c. Subsequently, sample 2 underwent a TCLT, which replicated the stress conditions experienced by cement sheaths in multi-stage fracturing. Upon completion of the TCLT, sample 2 was also subjected to a permeability test, followed by a TCT. TCT, TCLT, and permeability tests were conducted under 10 MPa confining pressure. The implementation of TCT and TCLT was achieved with the MTS device, possessing a maximum load of 600 kN and a maximum hydrostatic pressure of 100 MPa.
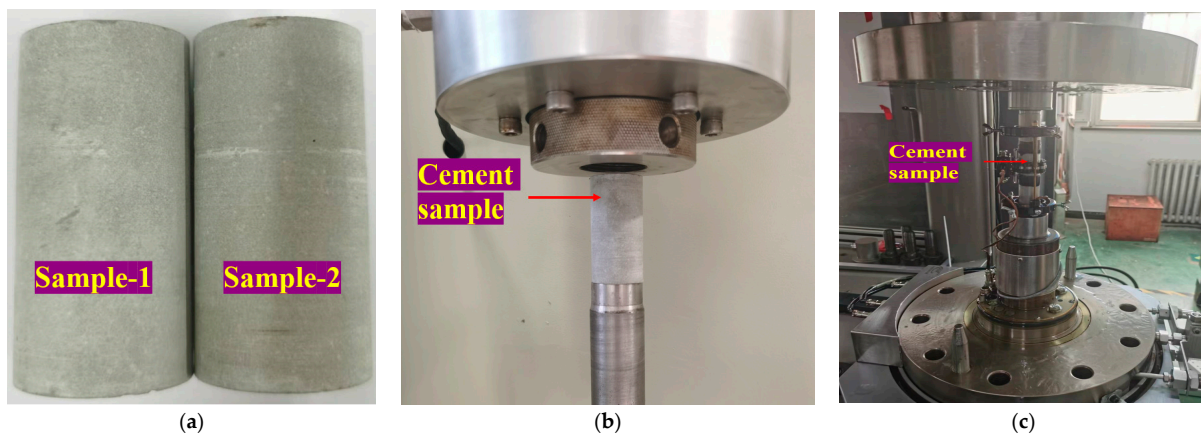

Figure 2. TCT, TCLT, and permeability test on cement samples: (**a**) samples 1 and 2, (**b**) permeability test, and (**c**) TCT and TCLT.

TCT procedure: The cement sample was placed within a pressure chamber, the triaxial cell. The employment of oil ensured the uniform application of confining pressure around the sample's lateral surface. On the premise of keeping the confining pressure constant, an axial load was gradually applied to the sample through a loading platen at the top. The applied load was increased until the sample failed.

TCLT procedure: With the triaxial cell, the cement specimen was enclosed in a rubber membrane to isolate it from the confining fluid. During the application of confining pressure, oil was employed to envelope the specimen. After reaching the desired initial confining pressure, cyclic axial loading was applied using a dynamic actuator. The cyclic loading was capped at 80% of the specimen's initial triaxial compressive strength over 15 cycles.

2.2. Experiment on the Cement Sheath Integrity

2.2.1. Experimental System

A comprehensive full-scale device was designed, comprising a foundation, a wellbore configuration, and an integrated control and data acquisition system. This device allows for simulation and evaluation of the cement sheath integrity under multi-stage fracturing. Notably, considering the exclusive detection of SCP in the B annulus under field conditions, the current experiments primarily focused on assessing the cement sheath integrity within this annulus. This device is depicted in Figure 3a, its structural layout is presented in Figure 3b, and the physical images are shown in Figure 3c,d.
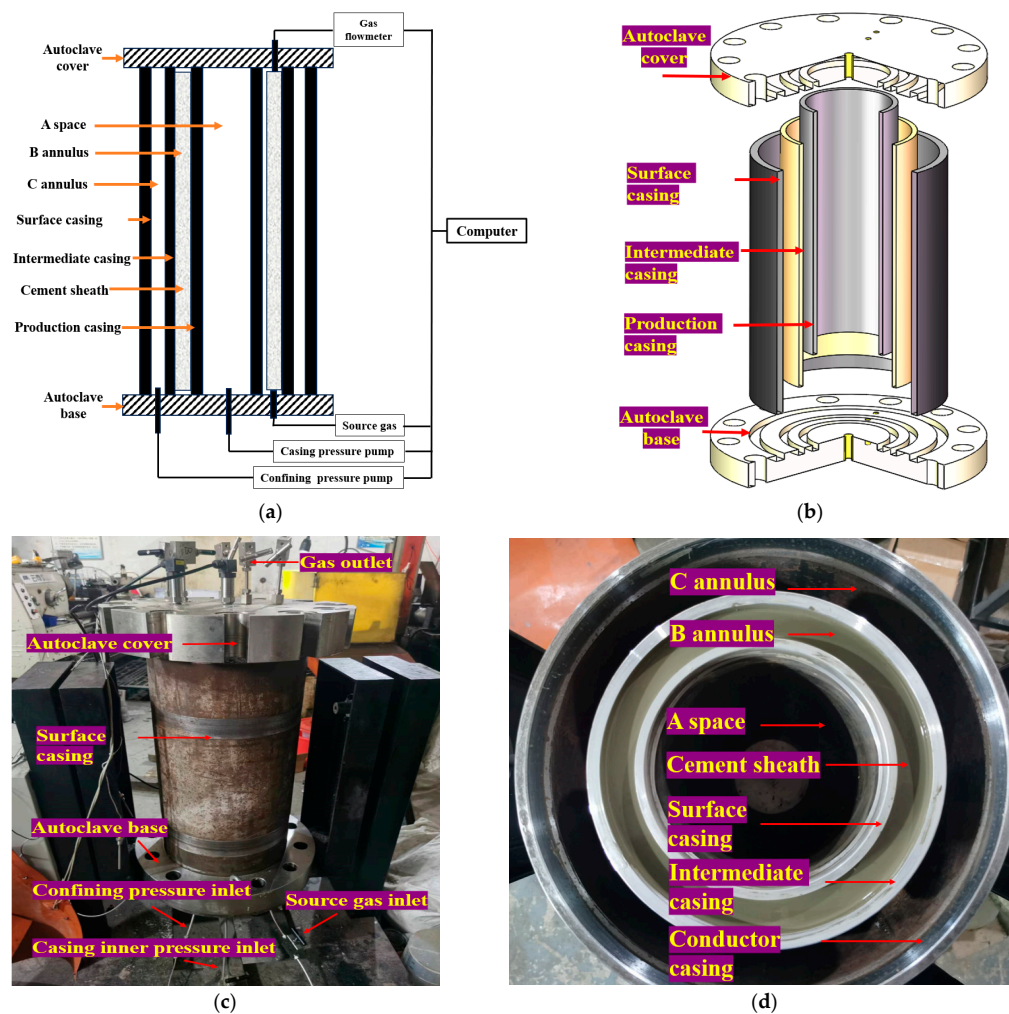
Figure 3. The full-scale device: (**a**) schematic diagram, (**b**) structural layout, (**c**) device assembled, and (**d**) casings.

Cement and casing materials for the experiments were obtained from the oil field. This practice ensured that the dimensions and materials of the inner and middle casings were precisely consistent with those used underground. The details of the casing system's specifications are provided in Table 1. Specifically, A space within the production casing was designated to provide cyclic pressure. In contrast, nestled between the production casing and intermediate casing, the B annulus served as cement injection to establish the cement sheath. Additionally, the C annulus, with its position between the surface casing and intermediate casing, exerted confining pressure and simulated the subterranean stress effects. This configuration guarantees that the experimental setup accurately replicates real-world field scenarios.

Table 1. Basic parameters of casings.

Casing	Grade	Diameter (mm)	Thickness (mm)
Surface casing	P110	177.8	9.19
Intermediate casing	P110	244.5	9.65
Conductor casing	N80	339.7	11.99

In this experiment, the adoption of a control system allows for the automated management of various modules, thereby ensuring the automation of the experimental procedure. Briefly, the control system guaranteed the source gas injection from the pump into the

cement sheath foundation; additionally, it continuously documented the data from the gas flowmeter at the upper side. Subsequently, the system sent commands to the confining pressure pump to apply the required pressure in the B annulus, thus simulating the geo-stress effects. Lastly, under the instruction of the control system, the casing pressure pump applied the required pressure precisely, creating cyclic pressure within the A space to replicate the multi-stage fracturing process. This automated workflow improved the experiment's safety, convenience, and accuracy.

Two-stage and three-stage cementing jobs are prevalent in cementing operations. Figure 4a,b depict their typical flowcharts. It can be seen that both processes are complex, leading to a prolonged duration. Bottom hole circulating temperature and bottom hole static temperature may impact the performance of cement slurries, potentially delivering adverse effects.
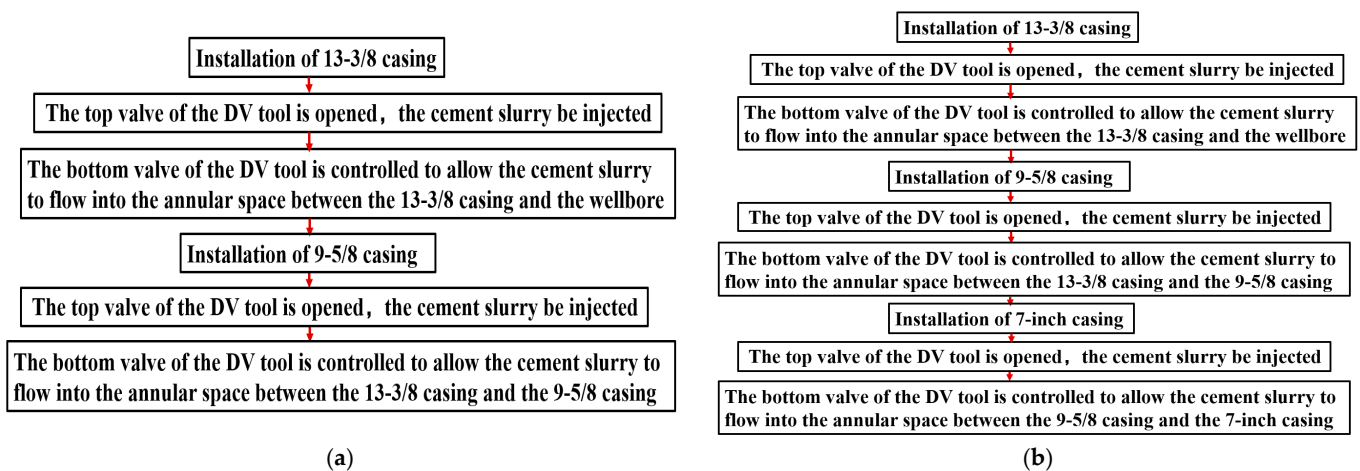

Figure 4. Diagrams of cementing jobs: (**a**) two-stage and (**b**) three-stage.

During the experiments, we prepared the cement slurry in a single batch and injected it into the annulus within five minutes. This short injection interval ensured consistent properties throughout, including rheology, permeability, and unconfined compressive strength.

2.2.2. Experimental Procedure

Based on the historical fracturing data from the A oil field, three distinct cyclic internal pressure groups featuring upper limit pressures of 70 MPa, 80 MPa, and 90 MPa were selected. The minimum threshold pressure for all cycles was standardized at 20 MPa, consistent with the hydrostatic pressure within the fracturing fluid. The detailed experimental protocol is outlined below:

(a) The casings from the oil field were installed, and the cement slurry was prepared according to the on-site cementing formula. Subsequently, the prepared slurry was injected into Annulus B with a 48 mPa·s plastic viscosity and a 15.3 Pa yield point.

(b) An upper autoclave cover was affixed to the top of the casing strings using bolts to maintain the integrity of the wellbore system. All necessary valves and sensors were connected. Confining pressure was applied to the C annulus via the confining pressure inlet to replicate the compressive force of formation acting on the casing. With the increasing well depth, the temperature of the geological formations rose continuously [33]. The system was heated to 60 °C with a heating jacket to simulate the geothermal temperatures. At this constant temperature, the cement was cured for 168 h, thereby creating a solid cement sheath [34].

(c) Test gas was pressurized to 2 MPa and introduced at the lower end of the B annulus. Cyclic internal pressures were applied using the casing inner pressure inlet under the instruction of the control system to mimic the multi-stage hydraulic fracturing operation. Each cycle was executed for 10 min, summing up to 15 cycles. In the event of a failure in

the cement sheath's integrity during the cyclic loading and unloading phases, test gas was prone to migrate from the annulus's base to its summit and exit through the gas outlet. The data acquisition system recorded the gas flow rate at the upper B annulus.

The flow chart of the experimental work methodology is shown in Figure 5:
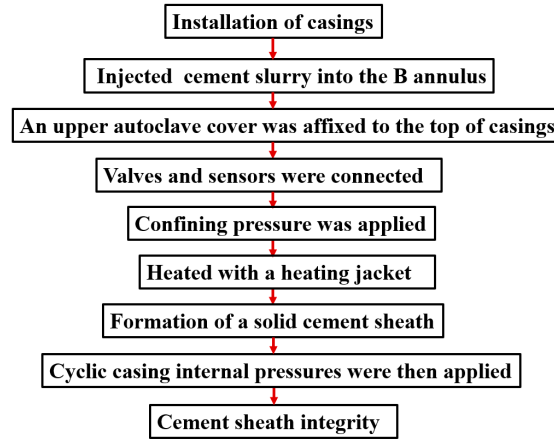

Figure 5. Flow chart of experimental methodology.

3. Numerical Simulation

Full-scale experiments have limitations in accurately simulating non-uniform geo-stress and capturing the evolution of micro-annulus widths during fracturing. For this consideration, a numerical model using ABAQUS 2022 finite element software was developed. The developed model helps elucidate the failure mechanism of the cement sheath integrity under multi-stage fracturing.

3.1. Finite Element Model

The simulation focused on the vertical section of Well H (Section A, located at a depth of 2000 m), as shown in Figure 6a. A comprehensive 3-D finite element model was constructed, comprising the production casing, B annulus cement sheath, intermediate casing, C annulus cement sheath, surface casing, and the surrounding formation, consistent with the actual dimensions of the wellbore. By employing structured and variable density meshing techniques, the model measures 5 m × 5 m × 5 m, as demonstrated in Figure 6b,c.
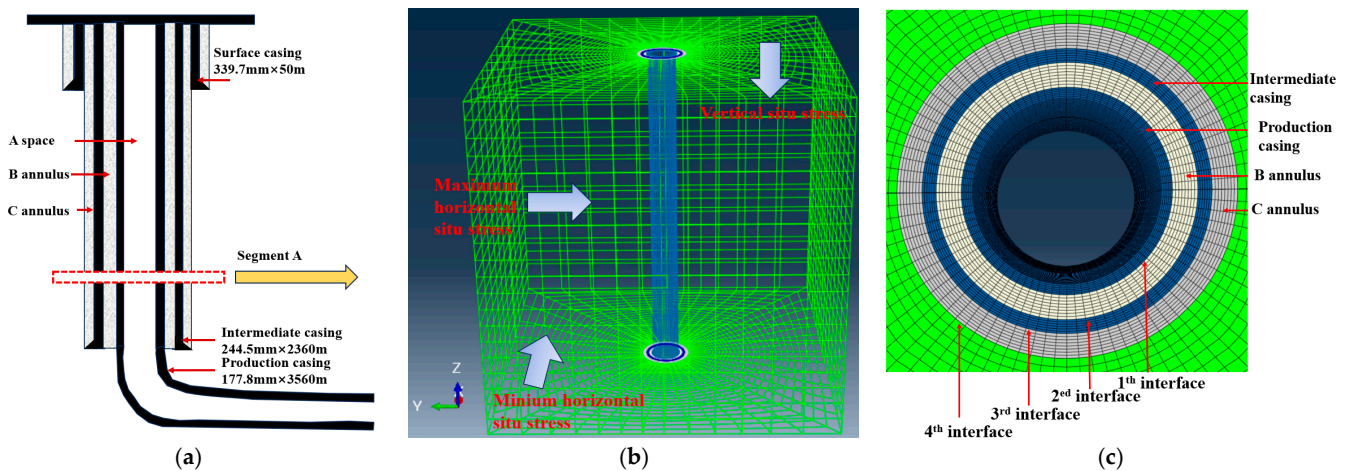

Figure 6. Finite element model based on actual wellbore structure: (**a**) structure diagram of the well, (**b**) finite element model, and (**c**) wellbore structure.

Regarding the simulated geo-stress conditions, the maximum and minimum horizontal principal stresses, along with vertical stress, were set at 26 MPa, 33 MPa, and 30 MPa,

respectively. The casing was represented through a linear elastic material model. Additionally, the cement sheath and formation were modeled using the Mohr–Coulomb constitutive model, with material specifics outlined in Table 2.

Table 2. Mechanical properties of cement, casing, and formation.

Name	Elastic Modulus (GPa)	Poisson's Ratio	Friction Angle (°)	Cohesive Strength (MPa)
Cement	12	0.23	25	9
Formation	23	0.18	30	6.2
Casing	210	0.28		

To simulate interface debonding, a zero-thickness cohesive element layer was inserted at the 1st, 2nd, 3rd, and 4th interfaces. The mechanical properties of these cohesive elements are detailed in Table 3. The maximum nominal stress damage criterion was used to judge the damage of the cohesive elements in this study, that is:

$$Max\left\{\frac{T_a}{T_a^0},\frac{T_b}{T_b^0},\frac{T_c}{T_c^0}\right\} = 1 \tag{1}$$

where T_a^0, T_b^0, and T_c^0 are the cohesive strengths in the normal direction, the first shear direction, and the second shear direction, respectively; T_a, T_b, and T_c are the interface stresses in the normal direction, the first shear direction, and the second shear direction, respectively.

Table 3. Mechanical properties of the cohesive elements.

Name	Normal Stiffness (GPa)	Shear Stiffness (GPa)	Normal Cohesive Strength (MPa)	Shear Cohesive Strength (MPa)	Critical Energy (J/m²)
The 1st, 2nd, and 3rd interface	0.8	2.2	1.2	2.3	100
The 4th interface	1.5	4.5	2.6	5.6	210

The BK fracture criterion was used in this study as the criterion for the damage evolution, that is:

$$\left\{\begin{array}{l} G^c = G_a^c + G_b^c + G_c^c \\ G_a^c + (G_s^c - G_a^c)\left\{\frac{G_b+G_c}{G_a+G_b+G_c}\right\}^\beta = G^c \end{array}\right\} \tag{2}$$

where G_a^c, G_b^c, and G_c^c are the critical energies needed for damage in the normal direction, the first shear direction, and the second shear direction, respectively; G_a, G_b, and G_c are the dissipation energies in the normal direction, the first shear direction, and the second shear direction, respectively; β is an empirical index.

3.2. Boundary Conditions and Simulation Steps

Initially, the finite element model was subjected to far-field geo-stresses to achieve a baseline equilibrium state. Subsequently, cyclic internal pressures were applied to the inner wall of the production casing to capture the actual construction parameters and replicate the fracturing experience. The number of circles was 15, with each involving pressurization and depressurization phases. Moreover, in line with the actual fracturing data from the A oil field, the internal pressure thresholds were set at upper limits of 70 MPa, 80 MPa, and 90 MPa and a lower limit of 20 MPa. The flow chart of the simulation work methodology is illustrated in Figure 7.
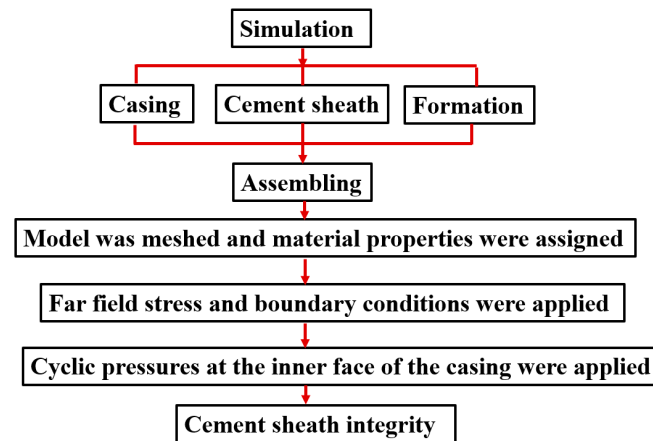
Figure 7. Flow chart of simulation work methodology.

3.3. Mesh Sensitive Analysis

A mesh sensitivity analysis on the model is typically necessary to mitigate the effects of mesh size on computational results [35]. In this process, mesh refinement and the subsequent coarsening around the wellbore when moving away from the well shaft reduce the total number of elements in the model, elevating computational efficiency. We adjusted mesh sizes near the wellbore to obtain different numbers of meshes and varying mesh divisions. On this basis, three configurations were detailed (refer to Table 4): coarse, medium, and fine. The coarse configuration comprises 16,371 elements, the medium configuration contains three times those of the coarse (49,152), and the fine configuration has seven times those of the coarse, totaling 114,600.

Table 4. Comparison of simulation results under different mesh sizes.

Configuration	Mesh Size of the Wellbore (mm)	Total Number of Meshes	Micro-Annuli Width (um)
Coarse	8	16,371	130.33
Medium	4	49,152	130.12
Fine	2	114,600	130

Numerical simulations were performed on the three mesh models under multi-stage hydraulic fracturing conditions at a maximum load of 70 MPa with 15 circles. The micro-annuli widths for the coarse, medium, and fine meshes at the 1st interface (Table 4) were 130.33 μm, 130.12 μm, and 130 μm, respectively. The relative differences between the coarse and medium meshes and between the medium and fine meshes were 0.16% and 0.09%, respectively, indicating the stability of calculations with the fine mesh. Moreover, the grid convergence index (GCI) was calculated [36]. The GCI values of the coarse and medium mesh groups (GCI_{21}) and the medium and fine mesh groups (GCI_{32}) accounted for 1.35% and 0.91%, respectively. These findings indicate that using a fine mesh reduces the computational results' dependence on mesh size, thereby confirming the accuracy and reliability of the numerical simulations with the fine mesh. Based on these analyses, we adopted this mesh without additional refinement, and all subsequent calculations will be derived from this fine mesh model.

3.4. Model Validation

Prior to conducting cement sheath integrity experiments, preliminary tests were conducted to evaluate the stability and safety of the experimental system. We chose 60 MPa as the upper limit for internal cyclic pressure across 16 cycles. As illustrated in Figure 8a, the test revealed a gas leak at 125 mL/min during the 15th cycle. The post-experiment

appearance of the cement sheath indicated the micro-annuli generation at the 1st interface, as shown in Figure 8b.
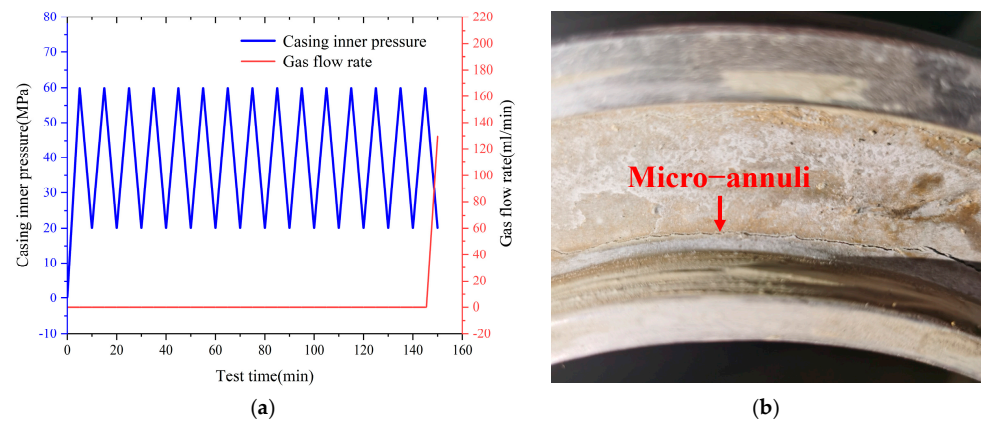

(a)

(b)

Figure 8. Results from the cement sheath integrity experiments: (**a**) experiment results and (**b**) morphology of cement sheath.

Using the established finite element model, we performed a numerical simulation of cement sheath integrity with an internal cyclic pressure limit of 60 MPa for 16 cycles. The simulation results showed that debonding occurred at the 1st interface during the 15th cycle, giving rise to micro-annuli formation. As detailed in Figure 9a, the morphology of the micro-annuli was measured at 82 μm in size. The casing was sectioned, and the micro-annulus was examined with a size of 88 μm using SEM, as shown in Figure 9b.
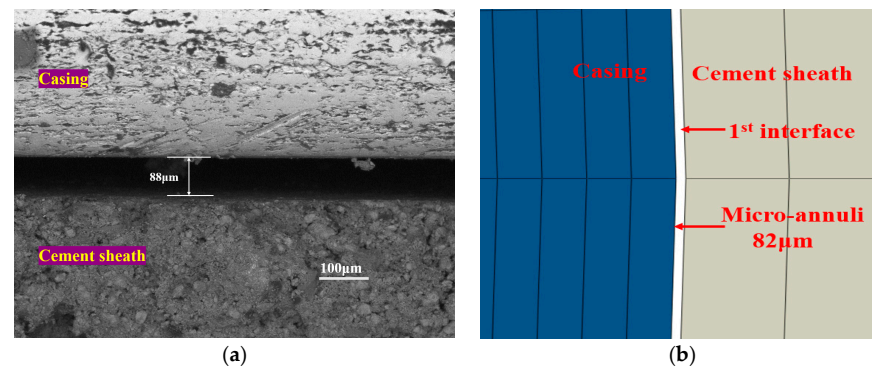

(a)

(b)

Figure 9. Microscopic morphology of micro-annuli: (**a**) experiment results and (**b**) simulation outcomes.

In numerical simulations and experiments, micro-annuli appeared at the 1st interface after loaded at the 15th cycle, and their widths were remarkably consistent. This consistency between the experimental results and numerical simulations confirms the effectiveness and reliability of the methods and models employed in this study.

4. Results and Discussion

4.1. Experimental Results

4.1.1. TCT, TCLT, and Permeability Test Results

The post-mechanical testing morphology of the cement samples is illustrated in Figure 10a, and the stress–strain curves before and after the TCT and TCLT are depicted in Figure 10b. The triaxial compressive strength, elastic modulus, and permeability before and after TCLT are detailed in Table 5. Initially, the cement's triaxial compressive strength and elastic modulus were 55 MPa and 7.2 GPa, respectively. The upper limit of cyclic loading was set at 44 MPa. After TCLT, the compressive strength and elastic modulus decreased by 10.7% and 8.3%, respectively, to 49.1 MPa and 6.6 GPa.
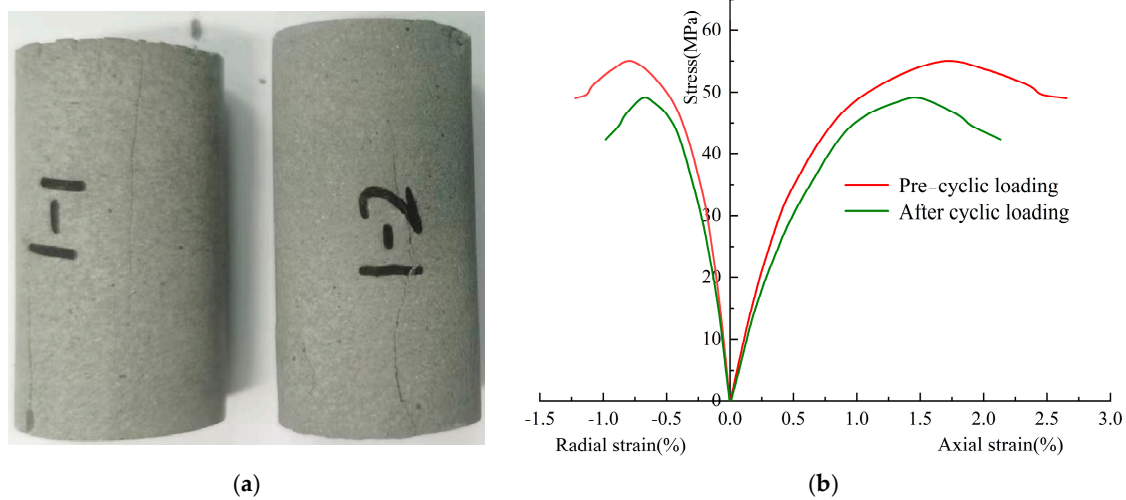
Figure 10. Results of mechanical testing on the cement samples: (**a**) morphology of the cement samples after testing and (**b**) stress–strain curves.

Table 5. Data on cement samples before and after TCLT.

Type	Triaxial Compressive Strength (MPa)	Elastic Modulus (GPa)	Permeability (mD)
Before TCLT	55	7.2	0.022
After TCLT	49.1	6.6	0.053

These changes imply microstructural damage in the cement, including elevated microcrack and microporosity densities, which reduced the matrix's load-bearing capacity, as evidenced by the decreased compressive strength and elastic modulus [37]. Nonetheless, these reductions were modest, suggesting that the cement retained its significant resilience to cyclic loading and its mechanical integrity under downhole fracturing conditions [38].

Following the TCLT, the permeability increased from 0.022 mD to 0.053 mD, reinforcing the observation that cyclic loading facilitated micropore and microcrack development, thereby enhancing permeability [39]. However, gas leakage through the cement matrix is only possible under permeabilities above 0.1 mD [40]. Consequently, the cement matrix maintained its seal integrity even after 15 TCLT cycles, suggesting unlikely bottom-hole gas leakage through the cement matrix, leading to SCP.

4.1.2. Stress–Strain Evolution in Cement under Cyclic Loading

Figure 11a illustrates the stress–strain curve of TCLT. Initially, the curve ascended near-linearly during the loading phase until reaching the predetermined upper-stress limit, triggering the commencement of unloading. The unloading phase featured a linear decrease until the stress diminished to the lower limit, at which point the cycle of reloading began. Each loading and unloading cycle contributed to the generation of new plastic strain, cumulatively increasing the total plastic strain. Notably, the loading and unloading curves collectively formed a hysteresis loop, which progressively shifted rightward with each cycle, indicating a gradual increase in accumulated plastic strain.

The dynamics of accumulated plastic strain throughout the TCLT are further detailed in Figure 11b. From the outset, the irreversible plastic strain (denoted as initial plastic strain) manifested in the 1st cycle at 0.5%. With the progression of cyclic loading and unloading, the magnitude of plastic strain grew steadily to 0.85% by the 15th cycle.

The above analysis reveals that the TCLT induces microstructural damage within the cement, resulting in irreversible plastic deformation. Moreover, as the TCLT cycles increased, the extent of microstructural damage also intensified, increasing the accumulated plastic strain.
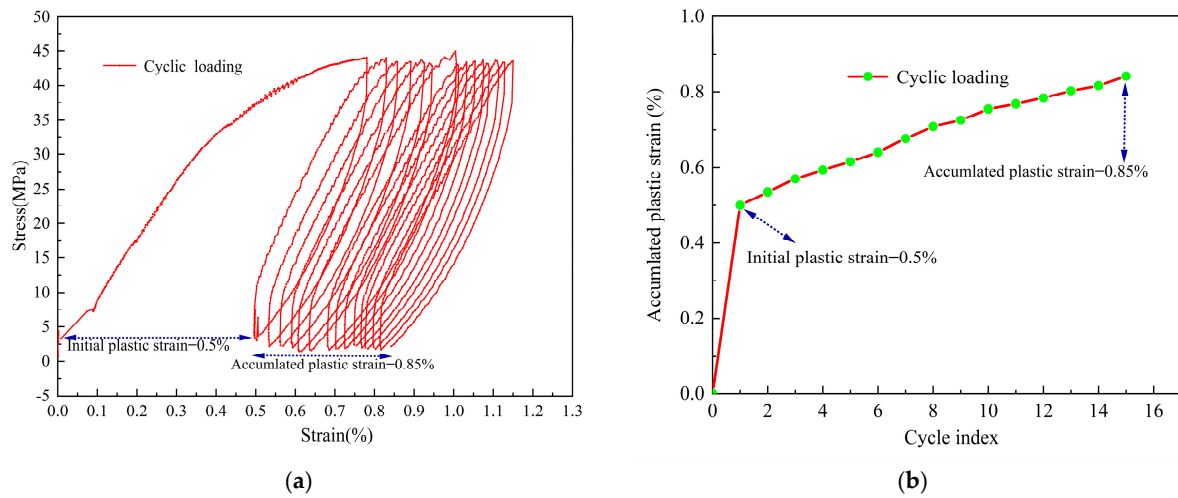
Figure 11. Results of cyclic loading: (**a**) cyclic loading curves and (**b**) cumulative plastic strain.

4.1.3. Cement Sheath Integrity Experiment Results

Figure 12 presents the results from three experimental groups, each showing changes in internal casing pressure and the monitoring gas flow rate at the top of the cement sheath over time. Gas leakage was observed at the 14th, 10th, and 8th cycles under upper limit pressures of 70 MPa, 80 MPa, and 90 MPa, respectively, solely during the depressurization phases. The initial leakage rates of the three groups were 151 mL/min, 160 mL/min, and 183 mL/min, respectively. As the cycles increased, the gas leakage rates rose progressively to 160 mL/min, 210 mL/min, and 235 mL/min, respectively, by the 15th cycle. These trends indicated that higher upper limit pressures in cyclic loading and unloading reduced the required cycles for cement sheath integrity failure, with the initial and final cycles resulting in increased gas leakage rates.
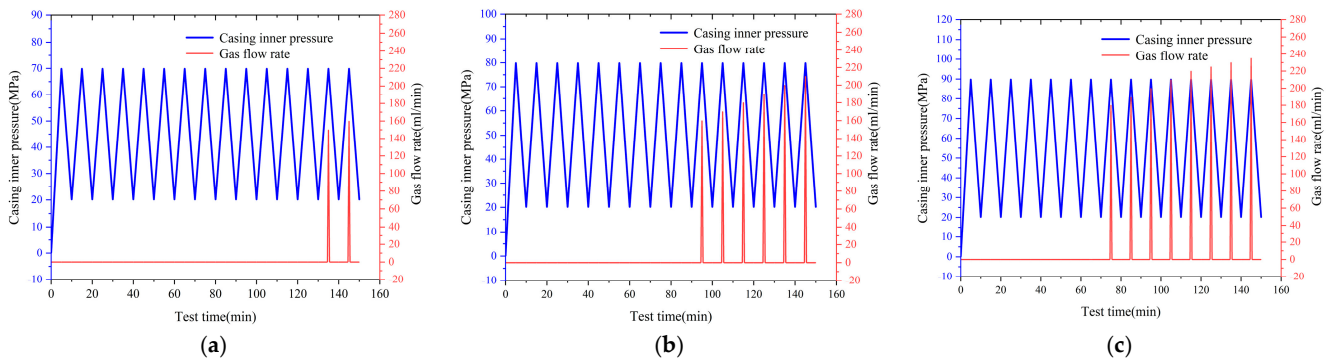

Figure 12. Results of the cement sheath integrity experiment: (**a**) 70 MPa, (**b**) 80 MPa, and (**c**) 90 MPa.

Figure 13 illustrates the morphology of cement sheaths following the three cyclic loading experiments. While no cracking was observed in any of the cement sheaths across the three experimental groups, distinct micro-annuli appeared at the 1st interface, in contrast to the well-bonded 2nd interface. Thus, cyclic loading induced cumulative plastic strain in the inner walls of the cement sheath at the 1st interface, which progressively increased with each cycle. In the depressurization phase, the inner walls could not return to their original shape, generating tensile stress at the 1st interface. Once surpassing the interface's bonding strength, this stress led to debonding and micro-annuli, serving as gas leakage conduits and causing SCP in the B annulus. Conversely, the 2nd interface showed no signs of debonding, likely due to lower stress levels that produced insufficient (minimal or none) cumulative plastic strain to initiate debonding. Gas leakage occurred solely during depressurization because the micro-annulus formation allowed the compressive forces

from the outer wall of the inner casing to close the micro-annuli. Consequently, gas from the bottom of the cement sheath could not breach the 1st interface. However, the micro-annuli reopened during depressurization, forming gas leakage pathways.
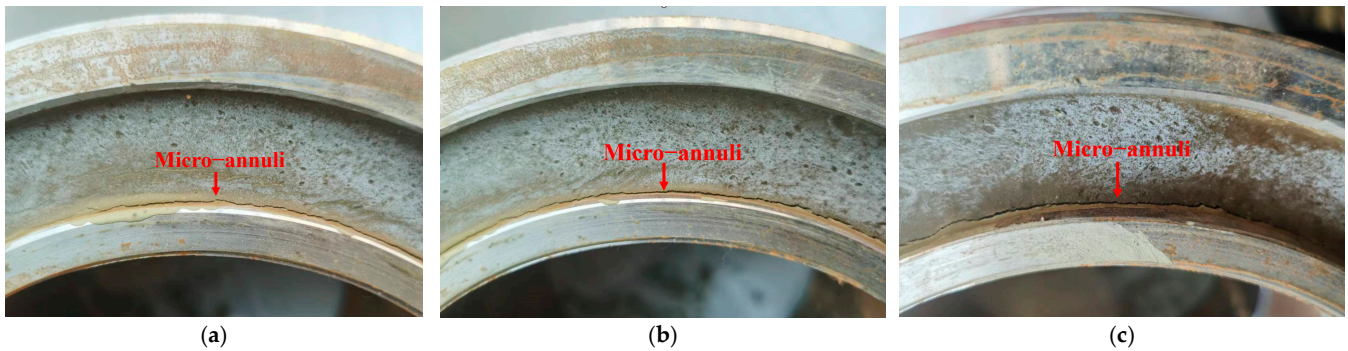

Figure 13. Morphology of cement sheaths: (**a**) 70 MPa, (**b**) 80 MPa, and (**c**) 90 MPa.

The casing and cement sheath with micro-annuli were meticulously sectioned, and their morphology was analyzed via SEM (Figure 14). Precise width measurements of the micro-annuli indicated that after 15 loading cycles under upper limit pressures of 70 MPa, 80 MPa, and 90 MPa, the widths reached 117 μm, 178 μm, and 212 μm, respectively. These results demonstrate that the widths of the micro-annuli increase with the upper limit pressure during cyclic loading. Thus, higher upper limit pressures induce more significant cumulative plastic strain on the cement sheath's inner walls, resulting in broader micro-annuli and, consequently, higher gas leakage rates.
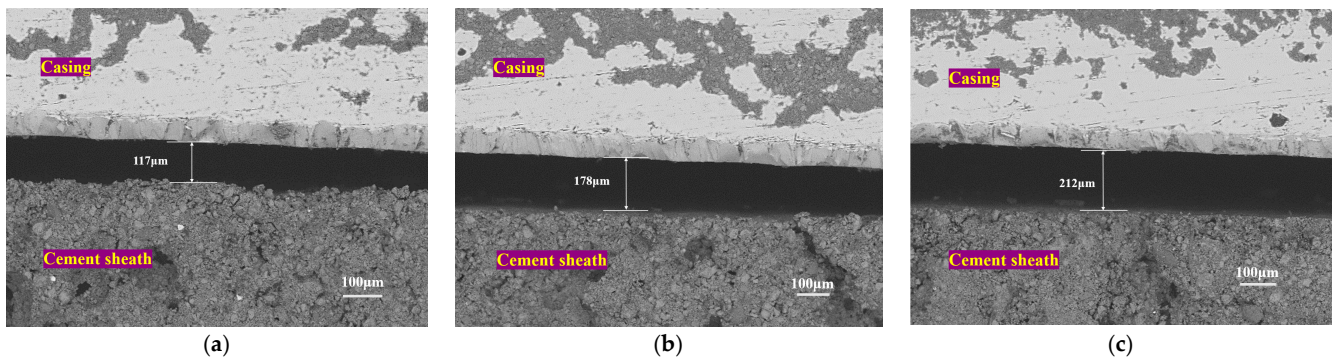

Figure 14. SEM results of the micro-annulus morphology: (**a**) 70 MPa, (**b**) 80 MPa, and (**c**) 90 MPa.

4.2. Numerical Simulation Results

4.2.1. Equivalent Plastic Strain Evolution in Cement Sheaths

The Plastic Equivalent Strain (PEEQ) quantifies the accumulated plastic strain following cyclic loading. PEEQ = 0 signifies no accumulated plastic strain, whereas PEEQ > 0 confirms its occurrence, with a larger PEEQ indicating a more significant accumulation. Figure 15 depicts the PEEQ distribution in the cement sheaths of the B and C annuli following 15 loading cycles. A marked plastic strain accumulation is observed in the cement sheath of the B annulus, whereas the C annulus exhibits no such strain. Despite unequal horizontal principal stresses, the C annulus's cement sheath and the intermediate casing mitigate horizontal geo-stresses, whereas the primary source of accumulated plastic deformation in the cement sheath is the casing's internal pressure. As a result, PEEQ shows a relatively uniform circumferential distribution. Notably, the highest PEEQ values are at the 1st interface, diminishing progressively toward the 2nd interface, with the 3rd and 4th interfaces exhibiting zero PEEQ values.

Figure 16 illustrates the PEEQ variations at the 1st, 2nd, 3rd, and 4th interfaces of the cement sheath under cyclic loading, with upper limit pressures of 70 MPa, 80 MPa, and 90 MPa. The initial PEEQ values at the 1st interface were 0.31%, 0.53%, and 0.66%,

respectively, for each pressure setting during the 1st cycle. As the cycles increased, the PEEQ values rose almost linearly to 0.79%, 0.95%, and 1.13% by the 15th cycle. At the 2nd interface, the initial cycle's PEEQ values were 0.11%, 0.18%, and 0.23%, which increased to 0.26%, 0.32%, and 0.47% by the 15th cycle. These results demonstrate that the largest PEEQ increases occurred during the 1st cycle for both the 1st and 2nd interfaces, with the 2nd interface's PEEQ values significantly lower than those at the 1st, indicating lesser cumulative plastic strain. PEEQ values at the 3rd and 4th interfaces remained at zero throughout the whole process.
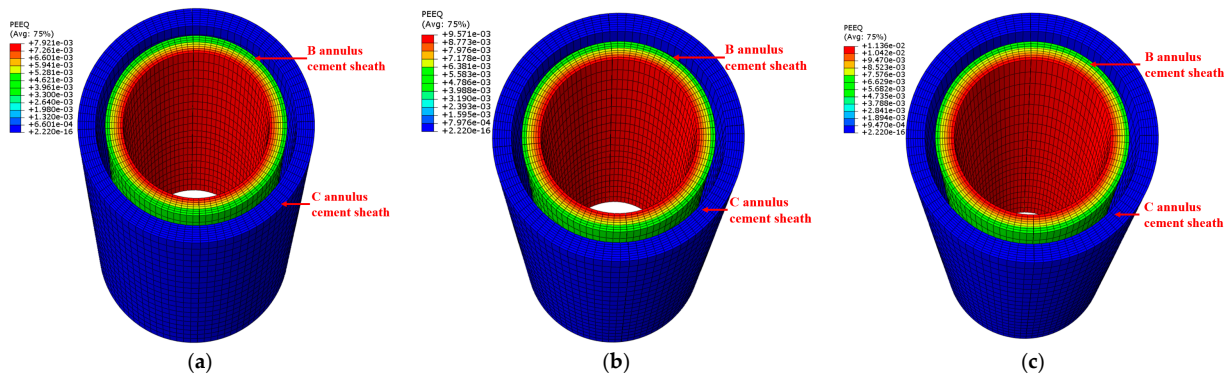

Figure 15. PEEQ distribution in the cement sheaths of the B and C annulus: (**a**) 70 MPa, (**b**) 80 MPa, and (**c**) 90 MPa.
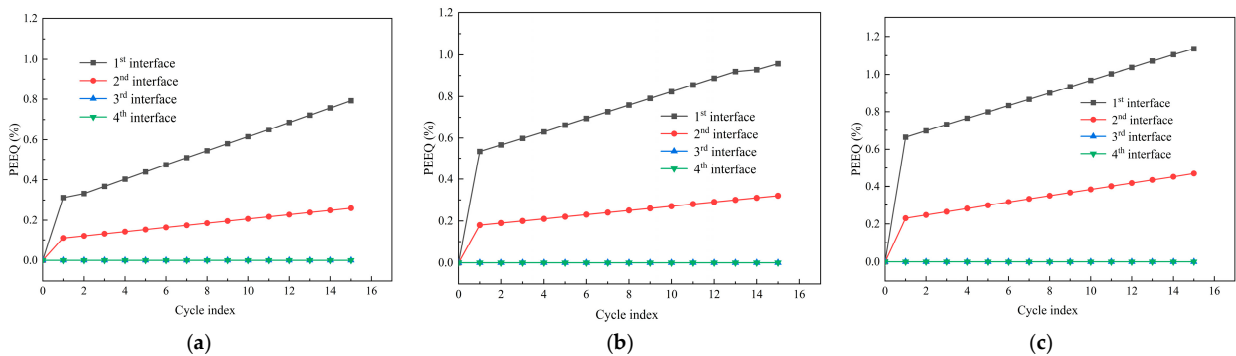

Figure 16. PEEQ evolution: (**a**) 70 MPa, (**b**) 80 MPa, and (**c**) 90 MPa.

4.2.2. Micro-Annulus Evolution at Interfaces

After 15 internal pressure cycles, the interface bonding states are illustrated in Figure 17. Micro-annuli were not observed at the 2nd, 3rd, and 4th interfaces but at the 1st interface.
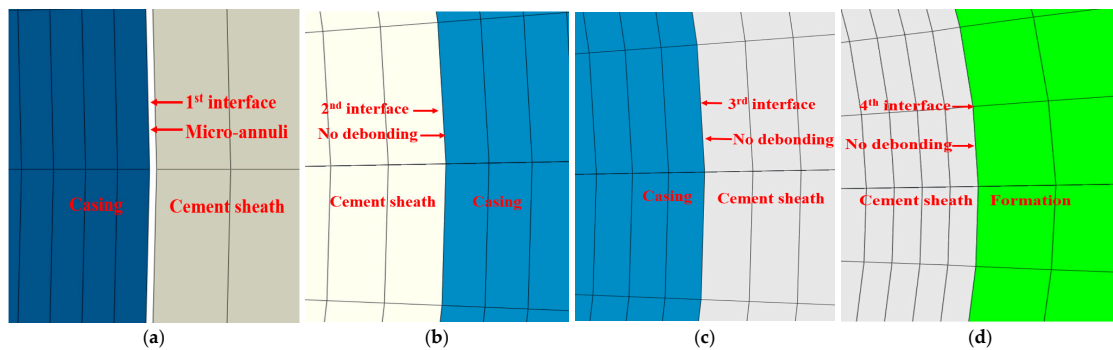

Figure 17. Debonding state at the interfaces: (**a**) the 1st interface, (**b**) the 2nd interface, (**c**) the 3rd interface, and (**d**) the 4th interface.

Post-processing of numerical simulation results yielded the circumferential widths of the micro-annuli at the 1st interface (Figure 18). Micro-annuli first appeared at the 8th, 10th,

and 14th cycles under upper limit pressures of 70 MPa, 80 MPa, and 90 MPa, respectively, with widths nearly uniformly distributed around the circumference. The initial widths of these micro-annuli were 83 μm, 95 μm, and 103 μm, respectively. As the cycles increased, the widths of the micro-annuli gradually expanded to 130 μm, 165 μm, and 205 μm by the 15th cycle, indicating that the largest width increase occurred during the initial appearance.
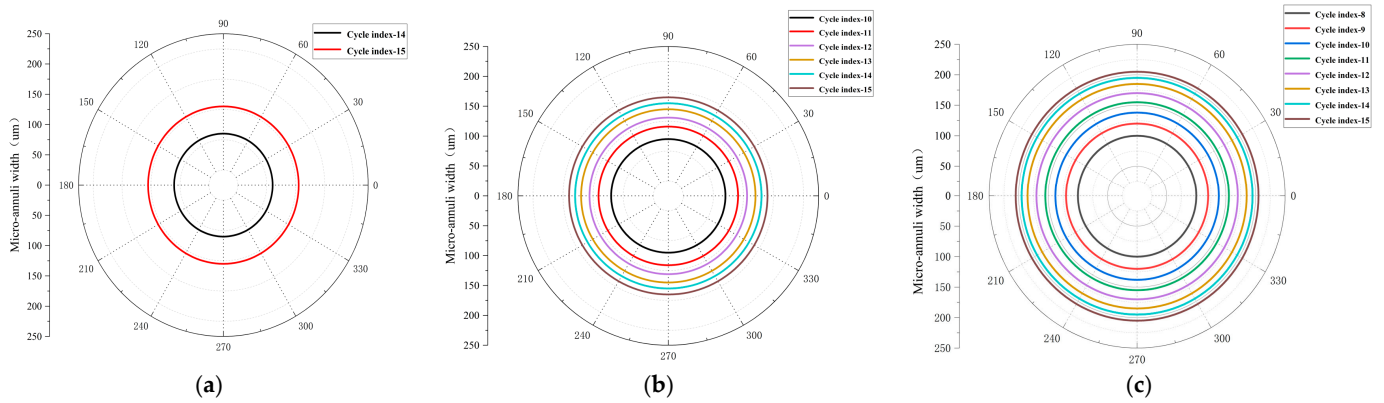

Figure 18. Evolution of micro-annulus width at the 1st interface: (**a**) 70 MPa, (**b**) 80 MPa, and (**c**) 90 MPa.

4.3. Correlation between Numerical Simulation and Experimental Results

The results of the three sets of experiments consistently demonstrated the presence of micro-annuli at the 1st interface. This finding was supported by the three sets of numerical simulations that also identified micro-annuli at the same location, confirming alignment between the numerically simulated and experimentally observed micro-annuli positions.

Experimental observations recorded gas leakage during the 8th, 10th, and 14th cyclic loading under upper pressure limits of 70 MPa, 80 MPa, and 90 MPa, respectively. Corresponding numerical simulations displayed micro-annuli at the 1st interface during identical cycles, corroborating the experimental findings. The agreement between the experimental cycles with gas leakage and the simulated cycles with micro-annuli substantiates the simulations' accuracy.

After 15 loading cycles, the experimentally measured widths of the micro-annuli were 117 μm, 178 μm, and 212 μm, respectively, closely mirrored by the simulation results of 130 μm, 165 μm, and 205 μm. This high degree of concordance underscores the consistency, stability, and reliability of this research.

4.4. Sensitivity Analysis

The mechanical properties of cement materials profoundly affect the stress level within the cement sheath. Choosing a cement formulation with suitable mechanical parameters can significantly reduce plastic deformation. This study performed a sensitivity analysis on four key mechanical properties, elastic modulus, Poisson's ratio, cohesive force, and friction angle, to guide future cement formulation designs. This analysis utilized a previously established finite element model, setting the casing's cyclic upper pressure at 70 MPa over 15 cycles.

Figure 19 depicts the PEEQ curves of cement sheaths under varying elastic moduli, where the PEEQ values increase progressively with the cycles, and both initial and final PEEQ values escalate as the elastic modulus increases. These observations suggest that cement with a lower elastic modulus can effectively reduce the risk of integrity failure in cement sheaths during multi-stage fracturing.

Figure 20 depicts the PEEQ curves under varying Poisson's ratios. Under the Poisson's ratios of 0.13, 0.18, and 0.23, the initial PEEQ values are 0.42%, 0.312%, and 0.09%, respectively, while the final PEEQ values are 0.51%, 0.79%, and 0.84%, respectively. These results demonstrate that cement with a higher Poisson's ratio helps reduce the stress level of the cement sheath during multi-stage fracturing.
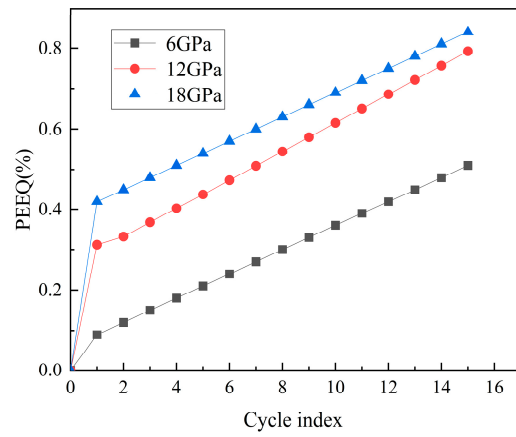
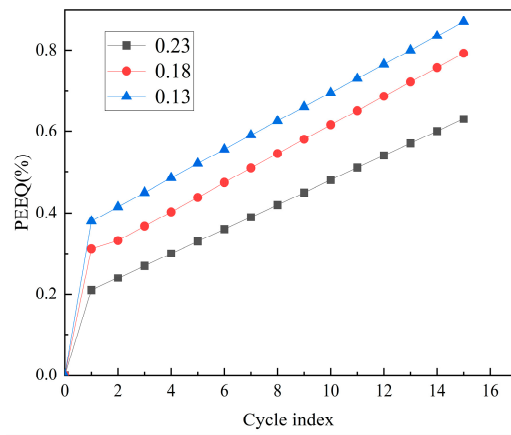**Figure 19.** PEEQ values under different elastic moduli.

Figure 20. PEEQ values under different Poisson's ratios.

Figure 21 illustrates PEEQ curves under varying friction angles. While both initial and final PEEQ values increase with the friction angle, the variations across different angles are not particularly significant. Nevertheless, a higher friction angle still benefits cement sheath integrity.
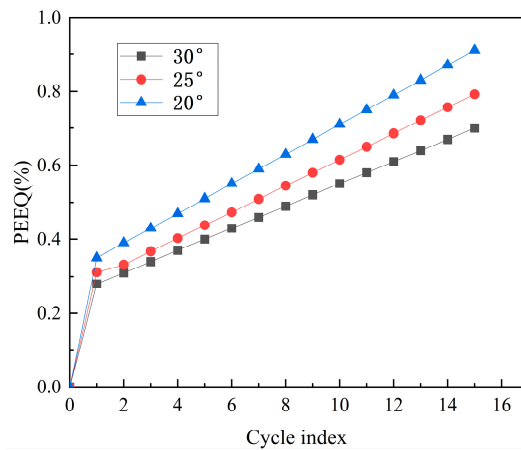

Figure 21. PEEQ values for different friction angles.

Figure 22 depicts the PEEQ curves under various cohesive strengths. The data indicate that at cohesive strengths of 5 MPa, 9 MPa, and 13 MPa, the initial PEEQ values are 0.14, 0.312, and 0.42, respectively, while the final values are 0.56%, 0.79%, and 0.84%. Thus, cement with a higher cohesive strength is advantageous for maintaining the integrity of the cement sheath during multi-stage fracturing.
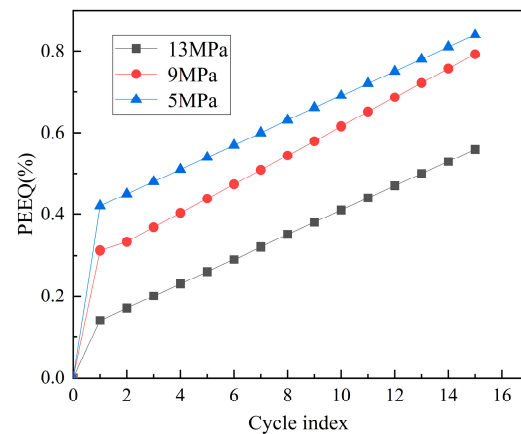
Figure 22. PEEQ values under different cohesive strengths.

4.5. Suggestions for Future Work

Experimental and numerical studies on cement sheath integrity revealed that during multi-stage fracturing, elevated cyclic pressure and increased cycling promoted micro-annulus formation, resulting in SCP. Therefore, it is essential to design the most appropriate multi-stage fracturing pressures and cycles based on the specific conditions of the formation and wellbore. Additionally, numerical simulations showed that cement mechanical properties significantly influence the plastic deformation extent of the cement sheath. When selecting cement materials, it is crucial to consider characteristics such as low elastic modulus, high Poisson's ratio, high cohesion, and high friction angle. Optimizing engineering parameters and choosing cement materials with superior properties are essential for enhancing wellbore integrity.

5. Conclusions

This research used the actual parameters from the A oil field in experiments and numerical simulations to investigate the integrity failures of cement sheaths during multi-stage fracturing, which uncovered the mechanisms behind these failures. The key findings are as follows:

Cyclic loading and unloading experiments on cement samples demonstrated cumulative plastic deformation in the cement, with triaxial compressive strength and elastic modulus decreasing by 10.7% and 8.3%, respectively, and permeability increasing by 150%. These results confirmed that cyclic loading caused micro-damage in cement. However, after 15 cycles, the permeability of the cement remained below the threshold for gas flow, indicating that gas would not leak through the cement sheath matrix underground.

Experiments with a full-scale device on cement sheath integrity under multi-stage fracturing confirmed that integrity failure was primarily due to micro-annulus formation at the 1st interface, attributed to cumulative plastic strain in the inner walls of the B annulus cement sheath during cyclic loading, leading to debonding at the 1st interface. While the outer wall of the B annulus cement sheath also experienced plastic strain, it was insufficient to cause debonding at the 2nd interface. No plastic strain was observed in the cement sheath of the C annulus, and no debonding occurred at the 3rd and 4th interfaces.

Both full-scale experiments and numerical simulations established that higher cyclic pressure limits resulted in fewer required cycles for cement sheath integrity failure, wider micro-annuli formation, and increased gas leakage rates through the interfaces.

The number of cycles for cement sheath integrity failure in the experimental groups matched perfectly with the cycles at which micro-annuli first appeared at the 1st interface in the numerical simulations. The measured widths of micro-annuli at the 1st interface were very close to those determined through numerical simulations, showing strong consistency between experimental and numerical results. These results validated the reliability of both approaches and provided valuable insights into the mechanisms of SCP generation

in offshore A oil field development wells, offering guidance for the design of offshore multi-stage fracturing parameters.

Author Contributions: Y.W.: conceptualization, methodology, software, validation, formal analysis, investigation, resources, and data curation. Y.F.: writing—original draft preparation, writing—review and editing, visualization, and supervision. All authors have read and agreed to the published version of the manuscript.

Institutional Review Board Statement: Not applicable.

Informed Consent Statement: Not applicable.

Data Availability Statement: The data presented in this study are available on request from the corresponding author.

Conflicts of Interest: The authors declare no conflicts of interest.

References

1. Qiu, K.; Fan, K.; Chen, X.; Lei, G.; Wei, S.; Navik, R.; Li, J. A New Approach for Production Prediction in Onshore and Offshore Tight Oil Reservoir. *J. Mar. Sci. Eng.* **2023**, *11*, 2079. [CrossRef]
2. Meng, M.; Ge, H.; Shen, Y.; Ji, W.; Wang, Q. Rock fabric of tight sandstone and its influence on irreducible water saturation in Eastern Ordos Basin. *Energy Fuels* **2023**, *37*, 3685–3696. [CrossRef]
3. Meng, M.; Zhang, Y.; Yuan, B.; Li, Z.; Zhang, Y. Imbibition Behavior of Oil-Saturated Rock: Implications for Enhanced Oil Recovery in Unconventional Reservoirs. *Energy Fuels* **2023**, *37*, 13759–13768. [CrossRef]
4. Meng, M.; Ge, H.; Shen, Y.; Ji, W.; Li, Z. Insight into water occurrence and pore size distribution by nuclear magnetic resonance in marine shale reservoirs, southern China. *Energy Fuels* **2022**, *37*, 319–327. [CrossRef]
5. Friesen, O.J.; Dashtgard, S.E.; Miller, J.; Schmitt, L.; Baldwin, C. Permeability heterogeneity in bioturbated sediments and im-plications for waterflooding of tight-oil reservoirs, Cardium Formation, Pembina Field, Alberta, Canada. *Mar. Petro-Leum Geol.* **2017**, *82*, 371–387. [CrossRef]
6. Wu, B.; Wu, G.; Wang, L.; Lou, Y.; Liu, S.; Yin, B.; Li, S. Study on fracturing parameters optimization of horizontal wells in low-permeability reservoirs in South China Sea. *Processes* **2023**, *11*, 2999. [CrossRef]
7. Du, F.; Huang, J.; Ru, X.; Ga, Y.; Yu, Z. Status and prospect of offshore horizontal well staged fracturing technology. *Offshore Oil* **2021**, *41*, 22–26. [CrossRef]
8. Liu, K.; Gao, D.; Taleghani, A.D. Analysis on integrity of cement sheath in the vertical section of wells during hydraulic fracturing. *J. Pet. Sci. Eng.* **2018**, *168*, 370–379. [CrossRef]
9. Chu, W.; Shen, J.; Yang, Y.; Li, Y.; Gao, D. Calculation of micro-annulus size in casing-cement sheath-formation system under continuous internal casing pressure change. *Pet. Explor. Dev.* **2015**, *42*, 414–421. [CrossRef]
10. Arshad, W.; Khaqan, K. Understanding the Key Factors Affecting Well Integrity in Horizontal Well Multistage Hydraulic Frac-turing. In Proceedings of the SPE Middle East Oil, Gas and Geosciences Show and Conference, Manama, Bahrain, 19–21 February 2023. [CrossRef]
11. Zeng, Y.; Liu, R.; Li, X.; Zhou, S.; Tao, Q.; Lu, P. Cement sheath sealing integrity evaluation under cyclic loading using large-scale sealing evaluation equipment for complex subsurface settings. *J. Pet. Sci. Eng.* **2019**, *176*, 811–820. [CrossRef]
12. Jiang, H.; Ren, Z.; Xi, Y.; Liu, G.; Li, J. Analysis of dynamic thermal behaviors for multi-stage hydraulic fracturing treatments in horizontal shale oil and shale gas wells. *Appl. Therm. Eng.* **2024**, *240*, 122213. [CrossRef]
13. Arjomand, E.; Bennett, T.; Nguyen, G.D. Evaluation of cement sheath integrity subject to enhanced pressure. *J. Pet. Sci. Eng.* **2018**, *170*, 1–13. [CrossRef]
14. Su, D.; Li, Z.; Huang, S.; Wu, X.; Li, J.; Xue, Y. Experiment and failure mechanism of cement sheath integrity under development and production conditions based on a mechanical equivalent theory. *Energy Sci. Eng.* **2021**, *9*, 2400–2422. [CrossRef]
15. Zhang, W.; Eckert, A. Micro-annulus generation under downhole conditions: Insights from three-dimensional staged finite element analysis of cement hardening and wellbore operations. *J. Rock Mech. Geotech. Eng.* **2020**, *12*, 1185–1200. [CrossRef]
16. Goodwin, K.J.; Crook, R.J. Cement sheath stress failure. *SPE Drill. Eng.* **1992**, *7*, 291–296. [CrossRef]
17. Deng, K.; Yuan, Y.; Hao, Y.; Li, Z.; Lin, Y. Experimental study on the integrity of casing-cement sheath in shale gas wells under pressure and temperature cycle loading. *J. Pet. Sci. Eng.* **2020**, *195*, 107548. [CrossRef]

18. Su, D.; Li, Z.; Wu, X.; Li, J.; Sun, J.; Zheng, G. Cement Sheath Integrity Evaluation Under Multiple Cyclic Loading Using Mechanical Equivalent Experiment for Gas Storage Wells in Eastern China. In Proceedings of the International Conference on Offshore Mechanics and Arctic Engineering, Hamburg, Germany, 5–10 June 2022. [CrossRef]

19. Feng, Y.; Li, X.; Gray, K.E. Development of a 3D numerical model for quantifying fluid-driven interface debonding of an injector well. *Int. J. Greenh. Gas Control* **2017**, *62*, 76–90. [CrossRef]

20. Wang, W.; Taleghani, A.D. Impact of hydraulic fracturing on cement sheath integrity; A modelling approach. *J. Nat. Gas Sci. Eng.* **2017**, *44*, 265–277. [CrossRef]

21. Li, J.; Xi, Y.; Tao, Q.; Li, Y.; Qu, G. Experimental investigation and numerical simulation of the emergence and development of micro-annulus in shale gas wells subjected to multistage fracturing. *J. Nat. Gas Sci. Eng.* **2020**, *78*, 103314. [CrossRef]

22. Dahi Taleghani, A.; Li, G.; Moayeri, M. Smart expandable cement additive to achieve better wellbore integrity. *J. Energy Resour. Technol.* **2017**, *139*, 062903. [CrossRef]

23. Pereira, F.L.G.; De Simone, M.; Roehl, D. Wellbore integrity assessment considering casing-cement-formation interaction based on a probabilistic approach. In Proceedings of the 51st U.S. Rock Mechanics/Geomechanics Symposium, San Francisco, CA, USA, 25–28 June 2017.

24. Landry, G.; Welty, R.D.; Thomas, M.; Vaughan, M.L.; Tatum, D. Bridging the gap: An integrated approach to solving sustained casing pressure in the Cana Woodford shale. In Proceedings of the SPE Well Integrity Symposium, Galveston, TX, USA, 2–3 June 2015. [CrossRef]

25. Wu, X.; Li, Z.; Hou, Z.; Liu, J.; Huang, S.; Su, D.; Li, J.; Cao, C.; Wu, L.; Song, W. Analytical Perspectives on Cement Sheath Integrity: A Comprehensive Review of Theoretical Research. *ACS Omega* **2024**, *9*, 17741–17759. [CrossRef] [PubMed]

26. Rocha-Valadez, T.; Mentzer, R.A.; Hasan, A.R.; Mannan, M.S. Inherently safer sustained casing pressure testing for well integrity evaluation. *J. Loss Prev. Process Ind.* **2014**, *29*, 209–215. [CrossRef]

27. Al Ramadan, M.; Salehi, S.; Kwatia, G.; Ezeakacha, C.; Teodoriu, C. Experimental investigation of well integrity: Annular gas migration in cement column. *J. Pet. Sci. Eng.* **2019**, *179*, 126–135. [CrossRef]

28. Wolterbeek, T.K.; Cornelissen, E.K.; Nolan, S.; Todea, F.; Stam, W.; Roggeband, S.M.; Keultjes, W.J.G. Restoration of annular zonal isolation using localized casing expansion (LCE) technology: A proof of concept based on laboratory studies and field trial results. *J. Pet. Sci. Eng.* **2021**, *197*, 108103. [CrossRef]

29. Beltrán-Jiménez, K.; Skadsem, H.J.; Sunde, J.K.; Gardner, D.; Wolterbeek, T.K.; Cornelissen, E.K.; Keultjes, W.J. Restoration of annular zonal isolation using localized casing expansion (LCE) technology: Treatment of near-horizontal test sections containing a free-water channel. *J. Pet. Sci. Eng.* **2022**, *208*, 109792. [CrossRef]

30. Congro, M.; Skadsem, H.J.; Beltrán-Jiménez, K.; Roehl, D. Experimental and numerical study on the pushout shear strength of conventional and expanding cement–casing sections for well integrity. *Geoenergy Sci. Eng.* **2024**, *234*, 212638. [CrossRef]

31. Tabatabaei, M.; Santos, L.; Al Hassan, A.A.; Dahi Taleghani, A. Surface-modified graphite nanoplatelets to limit deteriorative impacts of oil-based mud residuals on cement bonding. *SPE Drill. Complet.* **2023**, *38*, 235–242. [CrossRef]

32. Corina, A.N.; Opedal, N.; Vrålstad, T.; Skorpa, R.; Sangesland, S. The effect of casing-pipe roughness on cement-plug integrity. *SPE Drill. Complet.* **2020**, *35*, 237–251. [CrossRef]

33. Khurshid, I.; Lee, K.J.; Choe, J. Analyses of thermal disturbance in drilling deep and high temperature formations. *Energy Sources Part A Recovery Util. Environ. Eff.* **2013**, *35*, 1487–1497. [CrossRef]

34. Xi, Y.; Li, J.; Tao, Q.; Guo, B.; Liu, G. Experimental and numerical investigations of accumulated plastic deformation in cement sheath during multistage fracturing in shale gas wells. *J. Pet. Sci. Eng.* **2020**, *187*, 106790. [CrossRef]

35. Ali, I.T.; Afgan, I.; Khurshid, I. Stratified Two-Phase Turbulent Pipe Flow Simulations. *Int. J. Adv. Sci. Eng. Inf. Technol.* **2022**, *12*, 1301–1311. [CrossRef]

36. Aycan, O.; Topuz, A.; Kadem, L. Evaluating uncertainties in CFD simulations of patient-specific aorta models using Grid Convergence Index method. *Mech. Res. Commun.* **2023**, *133*, 104188. [CrossRef]

37. Zhou, S.; Liu, R.; Zeng, H.; Zeng, Y.; Zhang, L.; Zhang, J.; Li, X. Mechanical characteristics of well cement under cyclic loading and its influence on the integrity of shale gas wellbores. *Fuel* **2019**, *250*, 132–143. [CrossRef]

38. Murphy, B.P.; Prendergast, P.J. Measurement of non-linear microcrack accumulation rates in polymethylmethacrylate bone cement under cyclic loading. *J. Mater. Sci. Mater. Med.* **1999**, *10*, 779–781. [CrossRef] [PubMed]

39. Rao, F.; Zhang, Z.; Ye, G.; Liu, J. Mechanical behavior and assessment of foamed cement paste under staged cyclic loading. *Mater. Struct.* **2021**, *54*, 182. [CrossRef]

40. Thorpe, A.K.; Duren, R.M.; Conley, S.; Prasad, K.R.; Bue, B.D.; Yadav, V.; Miller, C.E. Methane emissions from underground gas storage in California. *Environ. Res. Lett.* **2020**, *15*, 045005. [CrossRef]